

Extraction of domain-specific magnetization reversal for nanofabricated periodic arrays using soft x-ray resonant magnetic scattering

D. R. Lee,^{1,*} J. W. Freeland,¹ G. Srajer,¹ S. K. Sinha,² V. Metlushko,³ and B. Ilic⁴

¹*Advanced Photon Source, Argonne National Laboratory, Argonne, IL 60439*

²*Department of Physics, University of California, San Diego, La Jolla, CA 92093,
and Los Alamos National Laboratory, Los Alamos, NM 87545*

³*Department of Electrical and Computer Engineering,
University of Illinois at Chicago, Chicago, IL 60607*

⁴*School of Applied and Engineering Physics, Cornell University, Ithaca, NY 14853*

(Dated: November 17, 2018)

A simple scheme to extract the magnetization reversals of characteristic magnetic domains on nanofabricated periodic arrays from soft x-ray resonant magnetic scattering (SXRMS) data is presented. The SXRMS peak intensities from a permalloy square ring array were measured with field cycling using circularly polarized soft x-rays at the Ni L₃ absorption edge. Various SXRMS hysteresis loops observed at different diffraction orders enabled the determination of the magnetization reversal of each magnetic domain using a simple linear algebra. The extracted domain-specific hysteresis loops reveal that the magnetization of the domain parallel to the field is strongly pinned, while that of the perpendicular domain rotates continuously.

PACS numbers: 75.25.+z, 75.75.+a, 75.60.-d

Understanding the reversal mechanism of the magnetization in periodic arrays of submicron and nanoscale magnets is of both scientific and technological interest. Fundamental changes in the statics and the dynamics of magnetization reversal imposed by nanostructures enrich the physics of nanomagnetism. A precise control of magnetization reversal involving well-defined and reproducible magnetic domain states in nanomagnet arrays is key to future applications, such as high density magnetic recording¹ or magnetoelectronic² devices. To achieve this, topologically various nanomagnets, ranging from simple disks³ to more complicated rings⁴ or negative dots (holes)⁵, have been investigated. However, as rather well-defined but non-single magnetic domains (or domain states) form in complicated geometries, it becomes difficult to characterize precisely magnetization reversal involving each domain at small-length scales with either conventional magnetization loop measurements, such as magneto-optical Kerr effect (MOKE) magnetometry, or magnetic microscopy, such as magnetic force microscopy (MFM). Moreover, in large-area arrays typically covering areas of a few square millimeters, extracting overall domain structures during reversal from microscopic images is clearly unreliable. Though diffracted MOKE measurement has been proposed recently to deal with this problem, it is found to provide little quantitative information on magnetization reversal involving domain formation and is limited to micrometer-length scales.⁶

Such quantitative information is available using the technique of soft x-ray resonant magnetic scattering (SXRMS).⁷ This technique exploits strong enhancement of the magnetic sensitivity of scattering intensities when incident circularly polarized soft x-rays are tuned to an absorption edge of constituent magnetic atoms. SXRMS has been used to study the magnetic structure in magnetic thin films⁸ or periodic arrays of stripe domains or

nanolines⁹. In this paper we present a simple scheme to extract quantitatively domain-specific magnetization reversal for nanomagnet arrays from SXRMS measurements. For this purpose, sample rocking curves, yielding in-plane diffraction scans, have been measured and analyzed on the basis of our previous work performed in the hard x-rays.¹⁰ In order to obtain magnetic information, SXRMS peak intensities were measured by varying the applied field at different diffraction orders, whose scattering structure factors are different. This allows us to determine directly the magnetization reversal of each magnetic domain using a simple linear algebra. The basic idea of incorporating such nonuniform magnetic domains in scattering theory has been explored in our previous work on polarized neutron scattering.¹¹

For this study an array of permalloy (Ni₈₀Fe₂₀) square rings was fabricated by a combination of e-beam lithography and lift-off techniques. A standard silicon wafer was spin-coated with a double-layer positive-type e-beam resist, and the resist layer was then patterned by e-beam lithography. A 20-nm-thick permalloy film was deposited onto it using an electron-beam evaporator in a vacuum of about 10⁻⁸ Torr. The as-deposited unpatterned film was magnetically soft with coercive and uniaxial anisotropy fields of a few Oersteds. Finally, after ultrasonic-assisted lift-off, the square rings were arranged in an array of 2 × 2 mm².

Experiments were performed at sector 4 of the Advanced Photon Source.¹² Polarized soft x-rays at the beamline 4-ID-C were generated by a novel circularly polarized undulator that provided left- and right-circular polarization switchable on demand at a polarization > 96%. The photon energy was tuned to the Ni L₃ absorption edge (853 eV) to enhance the magnetic sensitivity. While a vacuum compatible sample stage was rotated, the diffracted soft x-ray intensities were collected by a

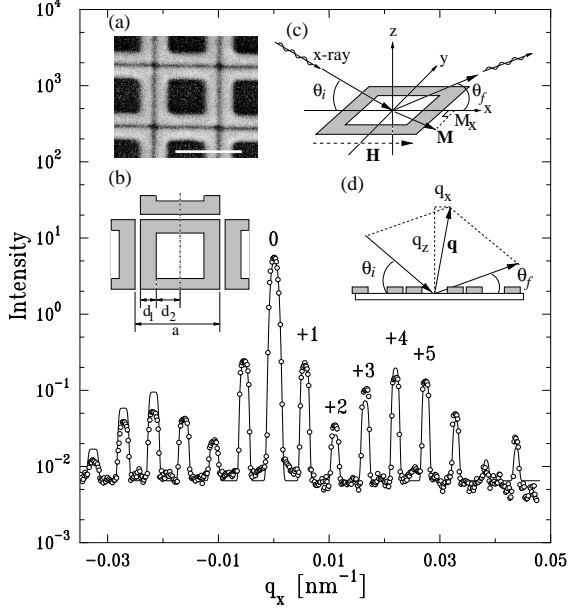


FIG. 1: Diffraction intensities of the rocking scan along the q_x direction at $q_z = 0.955 \text{ nm}^{-1}$ from a square ring array. Circularly polarized soft x-rays were used and the photon energy was tuned to the Ni L_3 absorption edge (853 eV). Circles represent measurements, and lines represent the calculations. Insets: (a) scanning electron micrograph and (b) schematic of the square ring array studied. The scale bar is $1 \mu\text{m}$. (c) and (d) show schematics of the scattering geometry, where θ_i and θ_f are the incidence and exit angles, and \mathbf{H} and \mathbf{M} are the applied field and magnetization, respectively.

Si photodiode detector with a fixed angle of 12.8° . This sample rocking scan, where the incident and exit angles θ_i and θ_f were varied with the total scattering angle ($\theta_i + \theta_f$) fixed, yielded a transverse q_x scan at a fixed q_z value (see Fig. 1). The angular resolution was defined by a pinhole between the sample and detector to be about 0.03° . The sample was mounted in the gap of an electromagnet that provides fields in the scattering plane of up to $\pm 800 \text{ Oe}$.

Figure 1 shows the diffraction intensities of the sample rocking scan measured as a function of q_x at $q_z = 0.955 \text{ nm}^{-1}$ from the square ring array with the saturation field. Diffracted intensities show peaks corresponding to an array period of $1.151 \mu\text{m}$. Following Refs. 10,11, the diffracted intensity I can be expressed in the kinematical approximation as

$$I(q_x; H) = |F(q_z)|^2 \sum_{n_x, |n_y|} \left| \rho_C F_C(n_x, |n_y|) + \rho_M F_M(n_x, |n_y|; H) \right|^2 \mathcal{R}(q_x; n_x, |n_y|), \quad (1)$$

where H is the applied field, $F(q_z)$ is the 1D form factor along q_z direction and consequently a constant value for a fixed q_z , and $F_{C(M)}$ and $\rho_{C(M)}$ are the charge (magnetic) form factors on the $q_x - q_y$ plane and the charge

(magnetic) contributions to the total atomic scattering amplitude, respectively. Near resonance energies ρ_M is proportional to the vector product $(\hat{\mathbf{e}}_f^* \times \hat{\mathbf{e}}_i) \cdot \mathbf{M}$,⁷ where $\hat{\mathbf{e}}_i$ and $\hat{\mathbf{e}}_f$ are unit photon polarization vectors for incident and scattered waves, respectively, and \mathbf{M} is the magnetization vector. For circularly polarized beams, this vector product reduces approximately to the component M_x in the inset (c) of Fig. 1. Therefore, the magnetization referred to hereafter represents strictly the parallel component to the x -axis or the field direction ($H \parallel \hat{x}$ in this study) of the magnetization vector. n_x, n_y are indices for Bragg points in the reciprocal space with the relationship of $q_{x,y} = (2\pi/a)n_{x,y}$, where a is the period of the array. Since the resolution function \mathcal{R} is a long thin ellipse oriented in the q_y direction, nonzero n_y values should also be taken into account for a q_x -scan performed at $q_y = 0$.^{10,11} We also note that the evolution of the peak widths of the different diffracted orders as a function of q_x , as shown in Fig. 1, was calculated using the model proposed by Gibaud *et al.*¹³

For a square ring, the charge form factor $F_C(n_x, |n_y|)$ can be expressed by

$$F_C(n_x, |n_y|) = \mathcal{C} \left[\text{sinc}(n_x(\gamma_1 + \gamma_2)) \text{sinc}(|n_y|(\gamma_1 + \gamma_2)) - \frac{\gamma_2^2}{(\gamma_1 + \gamma_2)^2} \text{sinc}(n_x \gamma_2) \text{sinc}(|n_y| \gamma_2) \right], \quad (2)$$

where \mathcal{C} is 1 for $|n_y| = 0$ and 2 for $|n_y| \neq 0$, and $\text{sinc}(x) = \sin(x)/x$. $\gamma_{1,2} = 2\pi d_{1,2}/a$, where d_1 and d_2 are the width of the ring and half of the inner square size, respectively, as shown in inset (b) of Fig. 1. Since F_C and F_M are the same functional forms for a saturated uniform magnetization, the diffracted intensities can be calculated using Eqs. (1) and (2) and are shown as the solid line in Fig. 1. From the best fit, d_1 and d_2 were estimated to be 162 ± 4 and $377 \pm 4 \text{ nm}$, respectively, and subsequently the gap between rings was 73 nm .

Figure 2 shows SXMRs peak intensities measured at various diffraction orders while field cycling. All field dependencies show magnetic hysteresis loops but with different features. This is due to different magnetic form factors for different diffraction orders, which reflect nonuniform domain formation during magnetization reversal, as pointed out in diffracted MOKE studies.⁶ Therefore, the magnetic form factor F_M in Eq. (1) should be expressed by the sum of the contributions of all possible magnetic domains, i.e.,

$$F_M(n_x, |n_y|; H) = \sum_l m_l(H) F_M^{(l)}(n_x, |n_y|), \quad (3)$$

where $m_l(H)$ represents the field-dependent magnetization of the l -th domain, which is the quantity of interest. It is noticeable that the magnetic factor in Eq. (3) can be factorized into the field- and structure-dependent factors. However, the domain-specific magnetization $m_l(H)$ cannot be directly extracted from measured SXMRs hysteresis loops because, as described in Eq. (1), the diffracted

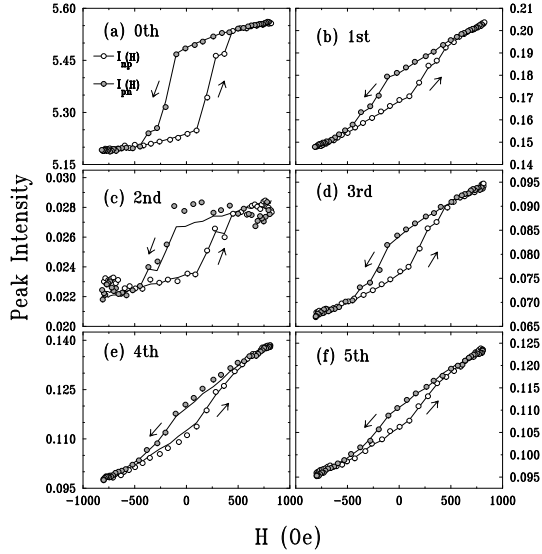


FIG. 2: SXRMS magnetic hysteresis loops (circles) measured at several diffraction peaks, indicated by numbers in Fig. 1. The solid lines represent the calculated hysteresis loops.

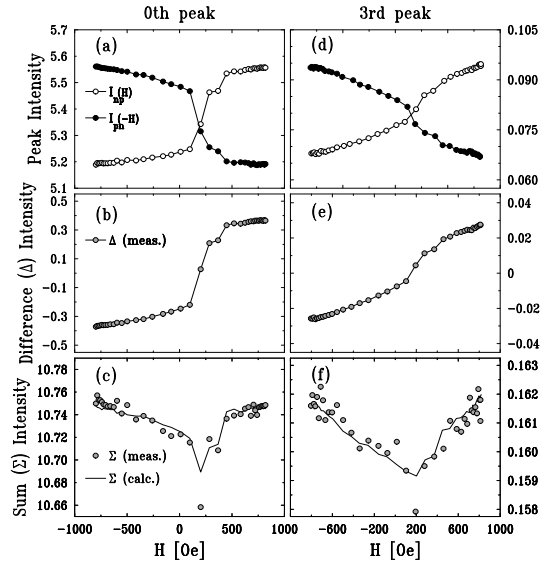


FIG. 3: (a) and (d) SXRMS hysteresis loops with positive-to-negative intensities (I_{pn}) flipped with respect to $H = 0$ for zeroth- and third-order peaks, respectively. Difference [(b) and (e)] and sum [(c) and (f)] intensities between $I_{np}(H)$ (negative-to-positive) and flipped $I_{pn}(-H)$ intensities as a function of the applied field. The solid lines in (c) and (f) represent the calculations.

intensities are the absolute square of the sum of the structural and magnetic contributions.

To tackle this problem, we considered the difference between the field-dependent intensities of $I_{np}(H)$ and $I_{pn}(-H)$, where I_{np} , I_{pn} represent the intensities measured while the field is swept along the negative-to-positive and positive-to-negative directions, respectively, and $I_{pn}(-H)$ represents the intensities flipped from

$I_{pn}(H)$ with respect to $H = 0$, as shown in Fig. 3. Assuming that the magnetization reversal has inversion symmetry about the origin, only the difference between $I_{np}(H)$ and $I_{pn}(-H)$ is the opposite sign of $m_l(H)$ in Eq. (3). However, this does not mean that they are symmetrical to a certain horizontal line in Fig. 3 (a) or (d) because the intensities contain quadratic terms to the magnetization $m_l(H)$, as described in Eq. (1), consequently leading to a nonsymmetry to the origin (or the center of mass) of SXRMS hysteresis loops in Fig. 2. This effect is clearly seen in the sum intensities of Figs. 3 (c) and (f) and will be an important characteristic of scattering-based hysteresis loops. However, in turn, these quadratic terms can be ruled out by taking the difference intensities, which are, as a result, linearly proportional to the magnetization.

These difference intensities at the n_x -order peak can be expressed from Eqs. (1) and (3) as

$$\begin{aligned} \Delta_{n_x}(H) &\equiv I_{np}(n_x; H) - I_{pn}(n_x; -H) \\ &= 4\text{Re}[\rho_C \rho_M^*] \mathcal{R}_{n_x} |F(q_z)|^2 \\ &\times \sum_l m_l(H) \sum_{|n_y|=0}^{\infty} F_C(n_x, |n_y|) F_M^{(l)}(n_x, |n_y|) \mathcal{R}_{n_y}, \end{aligned} \quad (4)$$

where \mathcal{R}_{n_x} and \mathcal{R}_{n_y} represent resolution functions evolving n_x and n_y indices, respectively, into which $\mathcal{R}(n_x, |n_y|)$ in Eq. (1) can be factorized. If we further normalize Δ_{n_x} by its maximum intensity with a saturation magnetization m_s , we can obtain a set of linear equations as

$$\frac{\Delta_{n_x}(H)}{|\Delta_{n_x}^{\max}|} = \sum_l B_{n_x l} \frac{m_l(H)}{m_s}, \quad (5)$$

where

$$B_{n_x l} = \frac{\sum_{|n_y|} F_C(n_x, |n_y|) F_M^{(l)}(n_x, |n_y|) \mathcal{R}_{n_y}}{\sum_{|n_y|} F_C^2(n_x, |n_y|) \mathcal{R}_{n_y}}. \quad (6)$$

Here we used the relationship of $\sum_l^{all} F_M^{(l)}(n_x, |n_y|) = F_C(n_x, |n_y|)$. Applying linear algebra, the normalized magnetizations $m_{l=1, \dots, N}(H)/m_s$ of N domains can be finally obtained directly from the normalized difference intensities $\Delta_{n_x}(H)/|\Delta_{n_x}^{\max}|$ measured at N different n_x orders by taking the inverse of $N \times N$ matrix $B_{n_x l}$.

In principle, the field-dependent intensities measured at semi-infinite numbers of orders can thus be used to determine the magnetization reversal of each infinitesimal cell in a unit nanomagnet. However, this is practically restricted due to finite measurable diffraction peaks and a high symmetry of experimental geometry. The latter gives rise to a strong dependence between $F_M^{(l)}(n_x, |n_y|)$ with different domain l or diffraction order n_x , and, as a result, makes the matrix $B_{n_x l}$ singular and noninvertible. To lower the geometrical symmetry of experimental configuration, we can use a vector magnetometry setup by rotating the sample/electromagnet assembly with respect to the incident photon direction.¹⁴ Since SXRMS

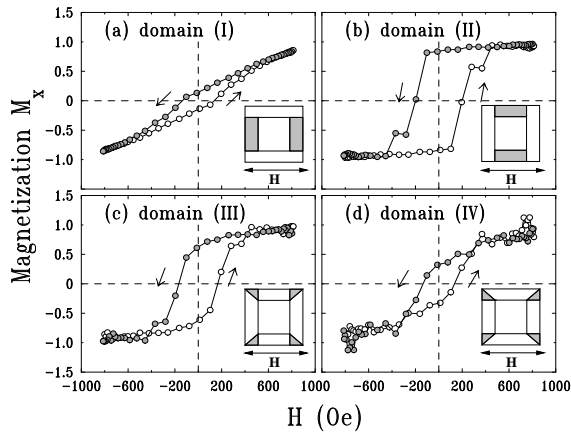


FIG. 4: Extracted magnetization reversals along the field direction of four types of characteristic domains, which are depicted as gray-filled regions in the insets, from SXRMS hysteresis loops at zeroth-, first-, third-, and fifth-order peaks.

intensities are proportional to the component of the magnetization vector along the projected incident photon direction onto the sample surface, this approach can also provide vectorial information about domain-specific magnetization.

In our setup, where both incident beam and field directions are parallel to one of the sides of the square rings, there may be four characteristic domains, as shown in the insets of Fig. 4. Each domain consists of two or four subdomains, whose structure-dependent form factors in Eq. (3) are identical, and, therefore, its magnetization represents an average value over subdomains. The explicit expressions of the structure-dependent magnetic form factors $F_M^{(l)}$ of these four domains for $(n_x, |n_y|)$ diffraction order in Eq. (3) will be presented elsewhere.¹⁵ We note that these domains have been chosen to minimize singularity of the matrix $B_{n_x l}$ and may not be thus energetically viable. Nevertheless, this scheme can unambiguously provide information about domain formation by considering snapshots of the resultant domain-specific magnetizations at each field.

To construct a 4×4 matrix $B_{n_x l}$ for four magnetic domains, at least four different peak intensities are re-

quired, and fifteen combinations can be allowed for six measured peaks, as shown in Fig. 2. However, we excluded the second peak due to its bad statistics and also some other combinations due to relatively small values of the determinants of their matrices $B_{n_x l}$, leading to a singularity of the matrix. For the optimum combination for non-singularity, zeroth-, first-, third-, and fifth-order peaks were then chosen. Figure 4 shows the finally extracted magnetization reversals for each domain using Eqs. (5) and (6). All magnetizations in Fig. 4 are normalized by the saturation and represent the components projected along the field direction, as discussed above, of the magnetization vectors. To confirm these results, the sum intensities in Figs. 3(c) and 3(f) and the SXRMS hysteresis loops for all observed peaks in Fig. 2 were also generated by substituting the results in Fig. 4 into Eq. (1). These calculations (solid lines) show a good agreement with the measurements.

A remarkable feature in the extracted magnetization reversals is that while the domain (I) perpendicular to the field rotates coherently, the parallel domain (II) is strongly pinned. Interestingly, this is similar to the domain behaviors in the antidot arrays,^{5,14} whose geometry resembles the square ring array except for narrow gaps between rings. On the other hand, the domain (II) clearly shows plateaus, which have been observed generally in circular or octagonal ring magnets and are attributed to the vortex state.⁴ A detailed discussion is beyond the scope of this paper and will be presented elsewhere.¹⁵

In summary, we successfully demonstrated that domain-specific magnetization reversals can be extracted directly from SXRMS hysteresis loops measured at various diffraction orders. Extracted domain-specific magnetization reversals are expected to provide a new insight into magnetic switching mechanism on nanofabricated arrays. Future studies, exploiting the element-selectivity and vector magnetometry setup, will provide further three-dimensional information in nanofabricated multilayers such as giant magnetoresistance and pseudospin valve structures.

Work at Argonne is supported by the U.S. DOE, Office of Science, under Contract No. W-31-109-ENG-38. V.M. is supported by the U.S. NSF, Grant No. ECS-0202780.

* Electronic mail: drlee@aps.anl.gov

¹ A. Moser *et al.*, J. Phys. D: Appl. Phys. **35** R157 (2002).

² S. Parkin *et al.*, P. IEEE **91**, 661 (2003).

³ R. P. Cowburn, J. Phys. D: Appl. Phys. **33** R1 (2000).

⁴ J. Rothman *et al.*, Phys. Rev. Lett. **86**, 1098 (2001); S. P. Li *et al.*, *ibid.* **86**, 1102 (2001).

⁵ R. P. Cowburn, A. O. Adeyeye, and J. A. C. Bland, Appl. Phys. Lett. **70**, 2309 (1997).

⁶ I. Guedes *et al.*, Phys. Rev. B **66**, 014434 (2002).

⁷ C. Kao *et al.*, Phys. Rev. Lett. **65**, 373 (1990).

⁸ J. M. Tonnerre *et al.*, Phys. Rev. Lett. **75**, 740 (1995); J. F. MacKay *et al.*, *ibid.* **77**, 3925 (1996); Y. U. Idzerda, V.

Chakarian, and J. W. Freeland, *ibid.* **82**, 1562 (1999); J. W. Freeland *et al.*, Phys. Rev. B **60**, R9923 (1999); J. B. Kortright *et al.*, *ibid.* **64**, 092401 (2001).

⁹ H. A. Dürr *et al.*, Science **284**, 2166 (1999); K. Chesnel *et al.*, Phys. Rev. B **66**, 024435 (2002).

¹⁰ D. R. Lee *et al.*, Appl. Phys. Lett. **82**, 982 (2003).

¹¹ D. R. Lee *et al.*, Appl. Phys. Lett. **82**, 82 (2003).

¹² J. W. Freeland *et al.*, Rev. Sci. Instrum. **73**, 1408 (2001).

¹³ A. Gibaud *et al.*, J. Phys. I **6**, 1085 (1996).

¹⁴ D. R. Lee *et al.*, Appl. Phys. Lett. **81**, 4997 (2002).

¹⁵ D. R. Lee *et al.*, in preparation.